

Intracavity Rydberg Superatom for Optical Quantum Engineering: Coherent Control, Single-Shot Detection, and Optical π Phase Shift

Julien Vaneecloo^{1,2}, Sébastien Garcia¹, and Alexei Ourjoumtsev^{1,*}

¹JEIP, UAR 3573 CNRS, Collège de France, PSL University,
11, place Marcelin Berthelot, 75231 Paris Cedex 05, France

²Sorbonne Université, 21 rue de l'École de Médecine 75006 Paris, France

 (Received 19 November 2021; accepted 23 February 2022; published 11 May 2022)

We demonstrate a new versatile building block for optical quantum technologies, enabling deterministic quantum engineering of light by combining the advantages of two complementary approaches: cavity quantum electrodynamics and interacting atomic ensembles. Our system is based on an intracavity Rydberg-blockaded atomic ensemble acting as a single two-level superatom. We coherently control its state and optically detect it in a single shot with 95% efficiency. Crucially, we demonstrate a superatom-state-dependent π phase rotation on the light reflected from the cavity. Together with the state manipulation and detection, it is a key ingredient for implementing deterministic photonic entangling gates and for generating highly nonclassical light states.

DOI: [10.1103/PhysRevX.12.021034](https://doi.org/10.1103/PhysRevX.12.021034)

Subject Areas: Atomic and Molecular Physics
Quantum Physics, Quantum Information

I. INTRODUCTION

Optical photons are a central physical resource in quantum technologies. Necessitating neither vacuum nor cryogenics to preserve their quantum features, they are essential for connecting distant quantum nodes, and they play a key role in quantum-enhanced sensing. However, assembling a quantum system capable of performing complex communication, calculation, simulation, or sensing tasks requires strong coherent interactions between its components, which photons do not easily provide.

For solving this longstanding issue, the most explored route consists in coupling photons to a highly anharmonic quantum system, most often epitomized by a single atom or a quantum dot, with an optical response strongly dependent on the number of photons it interacts with. This approach is very successful in the microwave domain, where the required anharmonicity is provided by circular Rydberg atoms [1] or Josephson junctions [2] coupled to superconducting resonators with very high quality factors. At optical wavelengths, to compensate for the relatively low transition dipoles, light fields need to be enhanced by confining the photons inside very low volume and high

finesse optical cavities [3–5]. A remarkable decades-long research effort in this direction [6,7] recently led to the first deterministic realizations of an optical two-photon quantum logic gate and of highly nonclassical optical Schrödinger's cat states [8,9]. Besides the difficulties in minimizing optical losses, reaching strong, steady, and reproducible couplings in such structures remains very challenging: By lack of optical access, real atoms are difficult to position precisely and to keep steady, while artificial atoms embedded in microstructures are strongly influenced by the surrounding substrate.

An alternative approach consists in injecting the photons in an atomic gas and transiently converting them into highly polarizable Rydberg polaritons [10,11]. This conversion is controlled by a laser beam driving the upper branch of a two-photon transition, creating an electromagnetically induced transparency (EIT) effect. Strong dipolar interactions between Rydberg atoms shift the energy of a pair out of the two-photon resonance. As a result, each polariton becomes surrounded by a blockade sphere where the EIT vanishes [12], which can be used to turn a coherent light beam into a stream of antibunched photons [13–15] and realize photon-controlled optical transistors [16,17]. Away from the single-photon resonance, this blockade effect modulates not only the dissipation but also the optical dispersion [18], allowing one to create bound photonic states [19–21] and to perform two-photon quantum logic operations [22]. Unfortunately, collisions between the Rydberg electron and the surrounding ground-state atoms [23] limit the maximal optical density per blockade sphere, which defines the transmission or phase contrast created by

*Corresponding author.

alexei.ourjoumtsev@college-de-france.fr

Published by the American Physical Society under the terms of the [Creative Commons Attribution 4.0 International license](https://creativecommons.org/licenses/by/4.0/). Further distribution of this work must maintain attribution to the author(s) and the published article's title, journal citation, and DOI.

a single Rydberg polariton. A conditional phase shift of π , required for most quantum logic and nonclassical light engineering tasks, is then accompanied by significant losses [24].

Here, we experimentally demonstrate that this goal can be reached with a platform combining the two previous approaches and enhancing the Rydberg blockade in a small atomic cloud with a single-ended medium-finesse optical cavity. We show that the cloud acts as a single Rydberg superatom with a collectively enhanced coupling to light, which we can coherently manipulate and optically detect in a single shot with 95% efficiency via the transmission of the cavity. Most importantly, with respect to recent experiments on Rydberg superatoms [25–28], where comparable efficiencies are reached, we successfully unlock a qualitatively new regime where the phase of the light reflected from the cavity is shifted by π by a single Rydberg excitation, allowing us to detect the latter with 90% efficiency via a homodyne measurement. This π phase rotation, together with the coherent control and the single-shot state detection, is crucial for implementing two-photon quantum gates [29] and for generating nonclassical optical resources for quantum sensing and communications.

II. STRONG SUPERATOM-PHOTON COUPLING

The central feature of our experimental setup is a small, cold ^{87}Rb ensemble in an in-vacuum, medium-finesse cavity, depicted in Fig. 1(a). This ensemble, with a Gaussian rms radius of $\sigma_a = 5 \mu\text{m}$, containing approximately $N = 800$ atoms at a temperature of $3 \mu\text{K}$, is prepared by sequentially cooling a background vapor in a two-dimensional magneto-optical trap (2D MOT), loading a 3D MOT, transporting atoms with a 1D moving optical lattice towards the cavity mode, further cooling by 3D degenerate Raman sideband cooling, loading in a crossed dipole trap, and pumping to the ground level $G:5S_{1/2}, F = 1, m_F = 1$ (details in the Appendix A). A 780-nm $D2$ and a 480-nm $109S$ beam resonantly drive two-photon transitions to the Rydberg state $R:109S_{1/2}, J = 1/2, m_J = 1/2, I = 3/2, m_I = 3/2$, with a detuning $\Delta/(2\pi) = -545 \text{ MHz}$ below the intermediate state $5P_{3/2}, F = 2, m_F = 2$. Interactions between Rydberg atoms, characterized at long range by the van der Waals coefficient $C_{RR} = 154 \text{ THz } \mu\text{m}^6$, shift the resonance of a Rydberg pair by $C_{RR}/r^6 > 2.4 \text{ MHz}$ for atoms separated by $r < 4\sigma_a$, a condition satisfied by more than 95% of atom pairs. This blockade of multiple Rydberg excitations makes the cloud behave as a two-level superatom with a ground state $|G\rangle$ and a state $|R\rangle$ corresponding to a single delocalized Rydberg $109S$ excitation.

The atoms are positioned at the $21\text{-}\mu\text{m}$ waist of a circularly polarized, running-wave, nearly Gaussian mode, defined by a single-ended four-mirror nonplanar cavity with a finesse $\mathcal{F} = 590$. This mode, driven by coherent

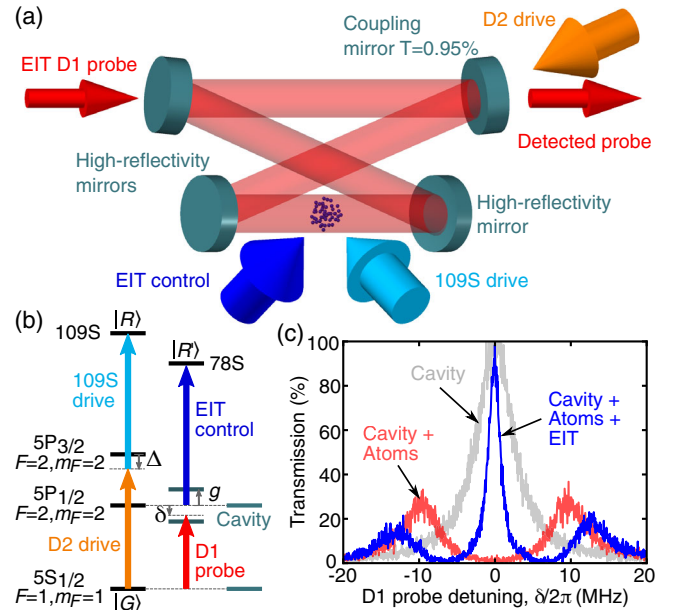


FIG. 1. (a) Experimental setup, configured for transmission measurement. (b) Level scheme. A small cloud of rubidium atoms behaves as a two-level superatom thanks to the Rydberg blockade. The $D2$ drive and $109S$ drive beams allow the excitation of the superatom to the $|R\rangle$ state. The atomic ensemble is strongly coupled to a medium-finesse cavity, resonant with the $D1$ line. The control beam enables the transmission of the $D1$ probe through the cavity by Rydberg EIT with the $78S$ state. (c) Cavity EIT spectra, where the transmission of the $D1$ probe, as a function of the probe detuning, is measured with a single-photon counting module (SPCM) and normalized to the maximum transmission of the empty cavity (light gray). With the strongly coupled atomic ensemble, we observe the vacuum Rabi splitting of the two transmission peaks, located at $\pm g/(2\pi) = \pm 10 \text{ MHz}$ (red). Adding the EIT control beam opens a transmission window at resonance (blue).

laser pulses, is resonant with the $D1$ -line transition from the ground state to the $5P_{1/2}, F = 2, m_F = 2$ level [see Figs. 1(b) and 1(c)]. The coupling mirror has a 0.95% transmission, allowing 90% of the photons to leave the cavity through this port. The atomic ensemble is collectively coupled to the cavity mode with a constant $g = 2\pi \times 10 \text{ MHz}$ exceeding the decay rates of both the cavity field ($\kappa = 2\pi \times 2.9 \text{ MHz}$) and the atomic dipole ($\gamma = 2\pi \times 3 \text{ MHz}$), leading to a vacuum Rabi splitting visible on the transmission spectrum [Fig. 1(b), red curve]. By adding a control laser coupling the $5P_{1/2}$ state to the $R':78S_{1/2}, J = 1/2, m_J = 1/2, I = 3/2, m_I = 3/2$ Rydberg state, we open an EIT window on resonance [Fig. 1(c), blue curve] and recover 90% of the bare cavity transmission for the $D1$ probe beam. This EIT window corresponds to a dark polariton state mixing a photon in the cavity with a Rydberg excitation $|R'\rangle$ in the cloud. Atoms in states R and R' interact strongly via their dipoles, in particular,

because this pair of states is close to a Förster resonance with the $110P_{3/2} + 77P_{3/2}$ pair. The asymptotic van der Waals scaling coefficient $C_{RR'} = 18 \text{ THz } \mu\text{m}^6$ overestimates the interactions in our parameter regime, but a complete diagonalization [30] gives an interaction-induced frequency shift of 3.4 MHz at the most likely distance $r = 2\sigma_a$. Therefore, a superatom in $|R\rangle$ efficiently shifts $|R'\rangle$ out of resonance, destroying the EIT and strongly changing the response of the system to the $D1$ probe, which drives the photonic component of the $|R'\rangle$ polariton.

III. CONTROL AND SINGLE-SHOT DETECTION

Figure 2 illustrates the single-shot detection of the superatom's state via the transmission of the $D1$ probe through the cavity. When the superatom is driven from $|G\rangle$ to $|R\rangle$, the EIT vanishes, and we observe a clear drop in the transmitted photon flux, detected with a fiber-coupled SPCM with a total detection efficiency of 47% [insets of Figs. 2(a) and 2(b)]. This flux can then be used to monitor Rabi oscillations of the superatom's state, driven with time-centered $D2$ and $109S$ beam pulses [Fig. 2(c)]. The former, which is shorter than the latter by $0.2 \mu\text{s}$, set the effective excitation duration t_d . One microsecond after the excitation is completed, we switch on the $D1$ cavity probe and integrate the transmitted photon detections over a time t_i , optimized as discussed below. From these single-shot results, we infer the statistic $|R\rangle$ population plotted in Fig. 2(c), where the probe power is set to obtain a 350-kHz count rate for a superatom in $|G\rangle$ and $t_i = 24 \mu\text{s}$. The dashed curve is the best fit by a sine function with a Gaussian decaying envelope, yielding the two-photon Rabi frequency $\Omega/(2\pi) = 1.5 \text{ MHz}$ and the e^{-1} Gaussian decay time $\tau_d = 2.8 \mu\text{s}$. The value of the Rabi frequency matches the expected behavior $\Omega = \sqrt{N}\Omega_{D2}\Omega_{109S}/(2|\Delta|)$, where the respective single-photon Rabi frequencies of the $D2$ and $109S$ drives $\Omega_{D2}/(2\pi) = 6 \text{ MHz}$ and $\Omega_{109S}/(2\pi) = 10 \text{ MHz}$ were determined independently and the \sqrt{N} scaling [31] was verified by partially depumping the atoms to the dark manifold $5S_{1/2}$, $F = 2$ and determining N from the vacuum Rabi splitting. The decay time τ_d is consistent with a motional dephasing of the polariton at $3 \mu\text{K}$ combined with 4%-rms fluctuations of Ω dominated by fluctuations on N , with calculated Gaussian decay times of $3.8 \mu\text{s}$ and $3.7 \mu\text{s}$, respectively.

Once the Rabi π pulse is calibrated, we can optimize the state detection. We first observe that the $|R\rangle$ state has a limited lifetime, visible as quantum jumps on individual SPCM records [see Fig. 2(b), inset] at $42 \mu\text{s}$ and as an exponential evolution on the mean rate [Fig. 2(d), red]. This effect limits the detection duration t_i because a quantum jump before t_i may induce a false-negative error. Increasing the input photon flux could make the detection faster, but we observe that the excited-state lifetime decreases proportionally (see Appendix B). This decrease may result from

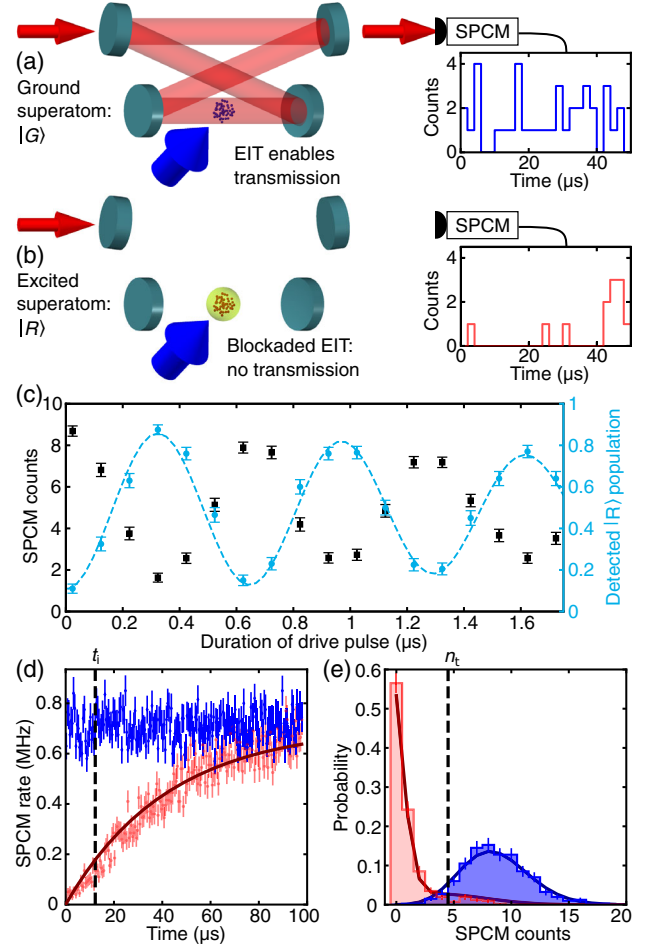


FIG. 2. Detection in transmission. The photon flux, detected with a SPCM, switches from (a) a high one without $109S$ Rydberg excitation to (b) quasizero with a single $109S$ excitation blocking the EIT (blockade sphere depicted in yellow). The insets show examples of single-shot measures with $2\text{-}\mu\text{s}$ binning. (c) The $109S$ Rabi oscillations visible on the averaged SPCM counts in the detection windows (black), and the $109S$ population deduced from single-shot detections (cyan). Each data point represents 200 detections. The dashed line is a best-fit Gaussian decoherence model. (d) SPCM count rate since the beginning of the probe $D1$ pulse without (blue) and with (red) a $109S$ Rydberg drive π pulse. The dark-red line is a best-fit exponential decay with a lifetime $\tau_R = 42 \mu\text{s}$. The dashed vertical line marks the end of the optimized detection window t_i . (e) Histograms of the number of photons, without (blue) and with (red) the π pulse. The dark curves represent modeled histograms. The dashed vertical line shows the optimized detection threshold n_t . (d,e) Data averaged over 400 repetitions. All error bars represent the standard error.

light-assisted collisions, which are difficult to model since each $109S$ atom has about 13 other atoms within the $2.8\text{-}\mu\text{m}$ LeRoy radius below which the $109S$ and $78S$ wave functions overlap significantly. This inverse proportionality relation effectively limits the number of photon counts providing a sufficiently low false-positive error probability ϵ_r . The photon flux will ultimately be limited by the

self-blockade of $|R'\rangle$ polaritons ($C_{R'R'} = 3 \text{ THz } \mu\text{m}^6$) and saturate towards about $1/(2\tau_p) = 6 \text{ MHz}$, with $\tau_p = 85 \text{ ns}$ the polariton lifetime, extracted from the EIT linewidth in Fig. 1(c).

The self-blockade makes the transmitted flux sub-Poissonian, with a measured zero-delay autocorrelation function $g^{(2)}(0) = 0.15$, but we recover $g^{(2)}(\tau) = 1$ for $\tau \gg \tau_p$. As we integrate the photon counts for at least a few microseconds, their statistic is quasi-Poissonian. Therefore, in Fig. 2(e), the histogram of single-shot SPCM counts n in a $t_i = 12 \mu\text{s}$ window with a ground-state superatom (blue) obeys $\mathcal{P}(n, t_i \phi_G) = e^{-t_i \phi_G} (t_i \phi_G)^n / n!$ (dark blue) with a mean count number of $t_i \phi_G = 8.7$, where ϕ_G is the average flux. When we apply a π pulse to excite the superatom to $|R\rangle$, the corresponding histogram (red) shows that most of the single-shot detections result in zero SPCM counts, as expected from the EIT blockade. The residual transmission results from three effects. First, finite-strength atom-light couplings and Rydberg interactions leave a residual transmitted flux ϕ_R . Second, even though the $|R\rangle$ lifetime $\tau_R = 42 \mu\text{s}$ largely exceeds t_i , quantum jumps to $|G\rangle$ occur within the detection window with a 25% probability. Third, the preparation efficiency η_R of $|R\rangle$, limited to $e^{-t_i/\tau_d} = 99\%$ by the duration t_i of the π pulse, contributes to the measured histogram. Thus, on the fitted model (dark red, see Appendix C) that accounts for these effects, we leave ϕ_R and η_R as free parameters, yielding the best-fit values $\phi_R/\phi_G = 4.5 \pm 0.4\%$ and $\eta_R = 100^{+0}_{-5}\%$.

Setting a detection threshold $n_t = 5$ (dashed line) in between the two distributions, with and without a π pulse, allows us to infer the most probable state of the superatom from a single-shot SPCM count n : $|G\rangle$ if $n \geq n_t$ or $|R\rangle$ if $n < n_t$. The integrals of the histograms, taken over $n \geq n_t$ with a π pulse and over $n < n_t$ without, give, respectively, the false-negative error $\epsilon_R = 4.8 \pm 1.1\%$ and the false-positive error $\epsilon_G = 5.3 \pm 1.1\%$. A conservative definition of the detection fidelity gives $\mathcal{F} = 1 - \max(\epsilon_G, \epsilon_R) = 94.7 \pm 1.1\%$, optimized by varying t_i and n_t . The resulting $t_i = 12 \mu\text{s}$ is a trade-off: Short times avoid errors induced by quantum jumps, while long times reduce errors through a lower uncertainty on the photon flux.

IV. OPTICAL π PHASE SHIFT

A cavity is optically far-overcoupled when the transmission of the input/output coupler greatly exceeds all other losses, and it is far-undercoupled in the opposite limit case. A resonant impinging beam is efficiently reflected in both cases, but with a π phase difference. In our case, for a superatom in $|G\rangle$, the EIT is good enough for the system to be overcoupled, while in $|R\rangle$, the blockade is sufficiently strong to switch the optical impedance to a far-undercoupled regime. We observe the expected π phase flip on a $D1$ probe reflected from the cavity using a balanced homodyne detection (HD) (see Fig. 3). The overall 75%

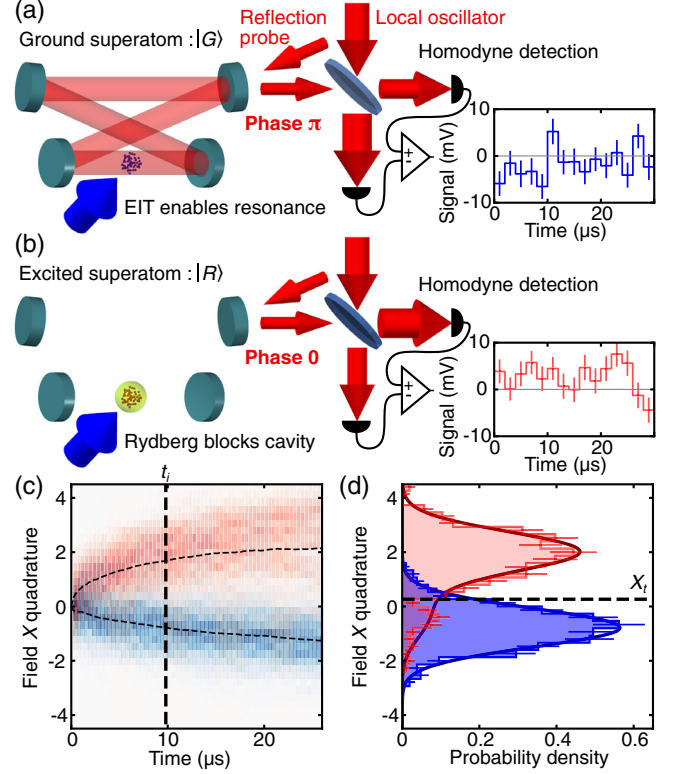


FIG. 3. The π phase shift in reflection. The reflected probe is combined with a local oscillator beam on a beam splitter, whose output intensity difference is measured by a HD setup. With the addition of a 109S Rydberg excitation blocking the EIT, the reflected probe phase changes from π (a) to 0 (b), resulting in a sign flip of the measured HD signal. The insets show examples of single-shot measures with a $2\text{-}\mu\text{s}$ binning. (c) In-phase quadrature X since the beginning of the probe $D1$ pulse without (blue) and with (red) a 109S Rydberg drive π pulse. The dashed lines indicate the quadrature means, and the colors represent the measured probability densities. The dashed vertical line gives the upper limit of the optimized detection window. (d) Histograms of the field X quadrature values, without (blue) and with (red) the π pulse. The dark curves represent modeled histograms. The dashed vertical line shows the optimized detection threshold. In panels (c) and (d), data are averaged over 400 repetitions. All error bars represent the standard error.

homodyne detection efficiency includes the optical losses outside the vacuum chamber, the mode-matching with the local oscillator, and the quantum efficiencies of the photodiodes, but it excludes all losses intrinsic to the cavity-superatom system. The phase of the probe relative to the local oscillator (LO) is stabilized by a lock-and-hold technique and referenced to a far-off-resonant cavity. For a superatom in $|G\rangle$, the system is resonantly excited, and we extract a phase $\theta_G = \pi(0.91 \pm 0.02)$ rad; for $|R\rangle$, the system becomes off-resonant, and we obtain $\theta_R = \pi(-0.045 \pm 0.013)$ rad, yielding a phase shift $\theta_G - \theta_R = \pi(0.96 \pm 0.03)$ rad.

As a first application, we use this phase flip to detect the superatom's state, via single-shot homodyne measurements

of the in-phase quadrature \hat{X} shown in Fig. 3(c), with the vacuum noise variance normalized to $1/2$. The input photon rate is at 580 kHz, on the edge of self-saturation effects, for which we observe a 38- μ s Rydberg lifetime. We reach a $89.9 \pm 1.5\%$ fidelity from the two measured density distributions in Fig. 3(d), for a 10- μ s integration time and a threshold set to $X_t = 0.27$. The fidelity is limited by the false-negative errors, while the false-positive probability value is $6.9 \pm 1.3\%$. We model these distributions as previously done (see Appendix B), taking into account the Rydberg state decay, and leaving as free parameters the preparation efficiency $\eta_R = 99_{-2}^{+1}\%$ and the reflectivity level for the superatom in the Rydberg state (red), $\mathcal{R}_R = 51 \pm 2\%$. The distribution for $|G\rangle$ is fitted by a Gaussian centered on the measured mean value (blue). This approach is more sensitive to probe self-saturation effects, directly decreasing the HD signal. Here, the self-blockade yields about a 7% effective reflectivity for $|G\rangle$ compared to $\mathcal{R}_G = 43 \pm 3\%$ in the low-intensity linear regime (see Appendix D).

V. CONCLUSION AND PERSPECTIVES

In conclusion, the demonstrated coherent state control, the two single-shot state detection methods, and the conditional optical π phase shift confirm that combining a Rydberg superatom with a medium-finesse cavity is a viable route towards deterministic optical quantum engineering. The state detection efficiencies match those recently obtained in Rydberg-based experiments operating in free space or in low-finesse resonators [26,27]. Unlike for single atoms, where intracavity absorption imaging provides much higher photon collection efficiencies than fluorescence imaging in free space, large scattering cross sections of Rydberg atoms enable absorption imaging in all circumstances: Here, the cavity enhances the contrast between the photon fluxes ϕ_G and ϕ_R but only weakly influences the detection efficiency. On the other hand, the π phase flip is a unique feature, relying on an excellent EIT combined with a strong Rydberg blockade, which would require postselection for free-space beams [24,32] and would vanish for a low- or high-finesse cavity. Indeed, a cavity with a lower finesse would require adding more atoms inside the Rydberg-blockade volume to keep the same level of optical undercoupling in $|R\rangle$. Ultimately, their number will be limited by the collisions between the Rydberg electron and ground-state atoms, which put an upper bound on the atomic density, and by the finite laser power and stray electric fields, which set a limit on the Rydberg principal quantum number and hence on the blockade volume. Conversely, for higher finesse cavities, the optical undercoupling in $|G\rangle$ will eventually be limited by finite mirror imperfections. Maintaining this undercoupling will also require improving the EIT by decreasing the number of atoms: A larger relative uncertainty on the latter will then result in larger fluctuations of the Rabi frequency.

In comparison with the well-explored, single-atom cavity QED route, our approach is still in its infancy. Nevertheless, it already offers a similar photon extraction efficiency [9] while having a considerable margin for improvement, even more so as in our setup we choose versatility over performance. For instance, cavity losses could be reduced by at least an order of magnitude by using superpolished mirrors with less broadband coatings and by cleaning the deposits that formed during the initial testing of the setup. Taking all sources of decoherence into account, we estimate that this improvement alone should increase the expected Choi-Jamiołkowski fidelity of a two-photon control-Z gate feasible with this setup from approximately 80% to approximately 95% [29]. The strong collective couplings of Rydberg-blockaded atomic ensembles allow the use of large cavities with nontrivial cavity geometries such as ours, which recently led to the first observation of optical Laughlin states [33]. The Rydberg-blockade mechanism could also be used to make neighboring superatoms interact with each other [34,35], opening countless possibilities for multimode quantum optics and quantum simulations.

ACKNOWLEDGMENTS

This work was funded by the Agence Nationale de la Recherche (ANR) Grant No. ANR-10-IDEX-001-02-PSL PISE, the CIFAR Azrieli Global Scholars program, and the ERC Starting Grant No. 677470 SEAQUEL. The authors thank P. Travers for technical support, S. Ćuk and M. Enault-Dautheribes for their assistance during the early stage of the project, and V. Magro for his help during characterization measurements.

Note added.—Recently, an experimental demonstration of a two-photon quantum logic gate using a setup very similar to ours was made public [36].

APPENDIX A: ATOMIC CLOUD PREPARATION AND DRIVING

The source of atoms is a sample of metallic rubidium heated at 37°C, providing a vapor pressure on the order of 10^{-7} mbar in a side vacuum chamber. In this side chamber, we create a two-dimensional magneto-optical trap (2D MOT) to cool ^{87}Rb with 50 mW of cooling laser light (red detuned by -10 MHz from the transition $5S_{1/2}, F=2 \rightarrow 5P_{3/2}, F=3$) and 0.4 mW of repumping laser light (resonant with the transition $5S_{1/2}, F=1 \rightarrow 5P_{3/2}, F=2$). With part of the cooling light, we push the cold atoms through a differential pumping tube into the main vacuum chamber containing the rest of the setup at a pressure of 2×10^{-9} mbar. The atomic beam loads a 3D MOT at a rate of 7×10^5 atoms per ms. The 3D MOT is formed by three pairs of orthogonal beams, each with a waist of 7.5 mm, 12 mW of cooling light (detuned by -18 MHz), and

0.2 mW of repumping light. The 8 G/cm magnetic field gradient is generated by a pair of in-vacuum coils in an anti-Helmholtz configuration. After 50 ms of loading, we compress the 3D MOT for 1 ms by ramping up the magnetic field to 21 G/cm. We follow this with a molasses phase for 2 ms, during which we ramp down the magnetic field and the beam intensities while increasing the detuning of the cooling light to -70 MHz.

The center of the 3D MOT is located 33 mm below the waist of the cavity mode. To transport atoms over this distance, we use a 1D-optical-lattice dipole trap as a conveyor belt for atoms [37]. The lattice is formed with two vertical counterpropagating laser beams at an identical wavelength of approximately 782.9 nm, each with a power of 0.25 W and a waist of 60 μm located midway between the 3D MOT and the cavity mode. We start by loading the lattice with atoms at the 3D MOT position during the molasses step. By linearly sweeping the frequency of one of the beams up and then down, we displace the interference fringes and thus the atoms trapped in maxima of light intensity. In 10 ms, we transport to the cavity center an ensemble of about 1 million atoms with a temperature of about 40 μK .

The thermal atomic motion has several detrimental effects. First, the Doppler broadening increases the transition linewidth to Rydberg levels, which reduces the EIT transparency. Second, the higher the temperature, the deeper a dipole trap has to be; thus, the differential light shift over the trapped cloud also broadens the transition linewidth to Rydberg levels. Third, the coherence of the Rydberg excited state of the superatom relies on the relative phases $\vec{k}_{\text{GR}} \cdot \vec{r}_i$ impinged by the exciting lasers, with a summed wave vector \vec{k}_{GR} , onto the atom i at position \vec{r}_i . The thermal motion thus induces a Gaussian decay of the coherence $e^{-t^2/\tau_{d,T}^2}$ at a characteristic time $\tau_{d,T} = \sqrt{m/k_B T / \|\vec{k}_{\text{GR}}\|}$, where m is the mass of the atom, k_B is the Boltzmann constant, and T is the temperature of the cloud.

In order to limit these effects, we implement degenerate Raman sideband cooling [38,39] once the atoms are at the cavity position. For this, we use a 3D optical lattice formed on the vertical axis with the conveyor belt lattice and in the horizontal plane by two independent and orthogonal interference patterns. The latter two are formed by two laser beam pairs whose waists are 0.17 mm and whose frequencies differ by 440 MHz and are blue detuned by 16 GHz from the transition $5S_{1/2}F=2 \rightarrow 5P_{3/2}F=3$. For one pair, the angle between the beam's wave vectors is 90° , while for the other pair, the angle is only 43° . Nevertheless, by adjusting the beam powers to approximately 3 mW and 10 mW, respectively, we obtain isotropic trapping sites whose oscillation frequency is 0.2 MHz. To do so, we measure the oscillation frequencies of each of the three orthogonal lattices by observing parametric heating losses when we modulate the beam intensities. The isotropic

oscillation frequency allows us to perform degenerate Raman sideband cooling in 3D. A magnetic field of 0.2 G brings to degeneracy the states $5S_{1/2}, F=2, m_F=2, n$ and $5S_{1/2}F=2, m_F=1, n-1$ with n the motional quantum number. Small angles of about 10° between the linear polarizations in each pair of beams induce Raman transitions from $5S_{1/2}, F=2, m_F=2, n$ to $5S_{1/2}, F=2, m_F=1, n-1$. A σ^+ -polarized Zeeman pumping beam with a 1-mm waist and 2 μW of power drives the transition $5S_{1/2}, F=2 \rightarrow 5P_{3/2}, F=2$ and, in the presence of a hyperfine repumper from $F=1$, brings the atoms back to the dark $m_F=2$ state. This transfer back to $m_F=2$ conserves the vibrational quantum number because we operate in the Lamb-Dicke regime where the recoil frequency of approximately 10 kHz is much smaller than the trap frequency of the lattice. The combination of Raman transitions and Zeeman pumping thus actively cools the atoms along all three dimensions. By applying this cooling for 5 ms to the atomic cloud inside the cavity, we reach a temperature of 1 μK . Several elements are crucial for minimizing this temperature. First, we pay special attention to the efficiency of the Zeeman pumping by using a clean, circular polarization and carefully aligning the magnetic field along the beam axis using microwave spectroscopy between the $F=1$ and $F=2$ hyperfine manifolds of the $5S_{1/2}$ ground state. Second, our horizontal lattice beams are relatively close to the $D2$ transition in order to get large dipole trapping frequencies with moderate beam intensities. Here, blue-detuned beams prove to be much more efficient for cooling than red-detuned ones, mainly because the trapping sites are at light intensity minima, thereby strongly reducing spontaneous emission. In addition, when atoms are trapped in near darkness, ac Stark shifts become negligible and do not affect the frequency of the Zeeman pump.

To achieve an efficient Rydberg blockade, we reduce the cloud's size by loading it in a crossed dipole trap formed by two orthogonal laser beams with approximately 20 mW of power at a 1064-nm wavelength with a 220-MHz frequency difference to avoid interference. Two in-vacuum aspheric lenses with 50-mm focal lengths and numerical apertures of 0.2 focus the two beams to about 15- μm waists at the cavity mode center. The trap loading is performed by alternating Raman cooling steps with compression steps, where we let cold atoms fall towards the trap center. In between these steps, we adiabatically ramp up or down the 3D lattice used for Raman cooling within 0.1 ms. After a final step of Raman cooling, we wait for 50 ms to let the cloud thermalize, which removes residual atoms with mechanical energies of the order of the trap depth. We end up with a cloud having a rms radius of 5 μm , containing about 800 atoms at a peak density of $4 \times 10^{11} \text{ cm}^{-3}$ and a temperature of 3 μK .

Before performing the experiments presented in the main text, the final step is to optically pump the cloud into the state $|G\rangle$ where the atoms are in the state

$5S_{1/2}, F=1, m_F=1$. At the beginning of this step, for $2 \mu\text{s}$, we apply a beam resonant with the transition $5S_{1/2}, F=2 \rightarrow 5P_{3/2}, F=2$ that pumps the atoms to $F=1$. A Zeeman pumping beam pumps them to $m_F=1$ during $100 \mu\text{s}$ by driving a σ^+ transition $5S_{1/2}, F=1 \rightarrow 5P_{3/2}, F=1$. The Zeeman pumping beam is circularly polarized and sent through the science cavity (about 200 MHz out of resonance) in the opposite direction to the probing beam used later. A 3-G quantization magnetic field is applied, with its direction quasialigned with the cavity-mode wave vector at the position of the atoms; the residual 12° angle stems from our beam geometry and ensures π -polarized transitions to Rydberg states. We perform microwave spectroscopy within the $5S_{1/2}$ manifold and find that the targeted $m_F=1$ state is populated at $95 \pm 2\%$, while the population in $m_F=0$ is $5 \pm 2\%$ and the population in $m_F=-1$ is negligible. With respect to $m_F=1$, the collective coupling strength of the population in $m_F=0$ is reduced by an order of magnitude by the lack of collective enhancement and because of a smaller transition dipole moment. Thus, we can consider the ensemble as efficiently described by a superatom in state $|G\rangle$.

To excite the superatom to $|R\rangle$, we use a $D2$ -drive circularly polarized beam that is spatially mode-matched and spectrally 200 MHz out of resonance with the fundamental mode of the science cavity, with a power of $2 \mu\text{W}$. The 109S driving beam, with a waist of about $60 \mu\text{m}$ and a power of 4 W, is produced in an in-vacuum build-up cavity in a confocal configuration. The build-up-cavity fundamental transverse mode is located 0.5 mm below the atomic cloud, and it allows us to lock the cavity on resonance with a beam detuned by one free spectral range (0.5 GHz). The 109S driving beam axis is orthogonal to the 3-G quantization magnetic field, and its polarization is aligned with the field, thus driving π transitions only towards Rydberg states. The $D2$ and 109S driving pulses are time centered and switched on and off using acousto-optic modulators (AOMs). Because the high-power 109S beam is less tightly focused in the AOM than the $D2$ probe, its switching time is slower. Therefore, we make the 109S pulse $0.2 \mu\text{s}$ longer than the $D2$ pulse, which sets the variable effective duration of the two-photon Rabi drive.

The 78S EIT control beam is produced with another in-vacuum build-up cavity, with a similar locking scheme, a similar waist, and a power of 5 W.

APPENDIX B: PROBE-DEPENDENT LIFETIME OF THE SUPERATOM EXCITED STATE

The lifetime of the superatom excited state $|R\rangle$ is a crucial parameter for the detection because quantum jumps out of $|R\rangle$ during the detection windows increase false-negative errors, thus reducing the detection fidelity. From the data in Fig. 4(a), we observe that this lifetime is clearly dependent on the transmission probe $D1$ intensity, which is

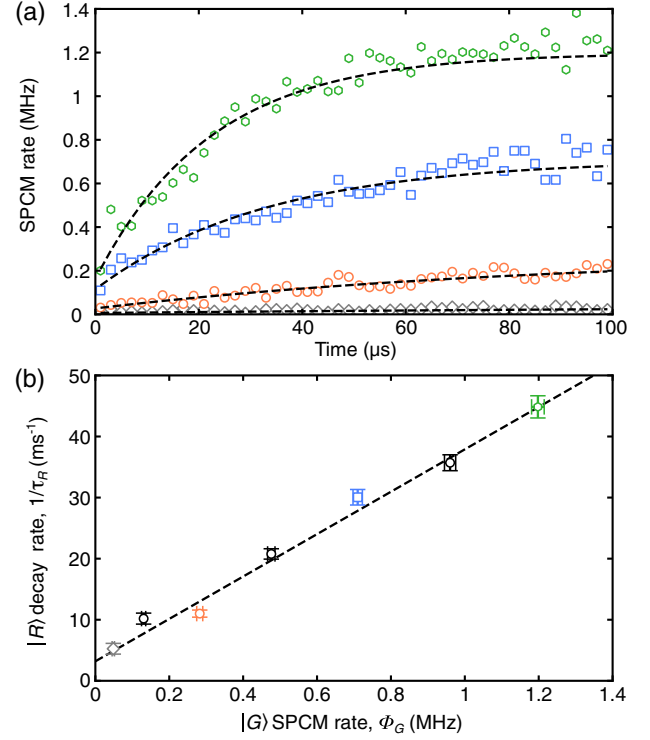


FIG. 4. Probe-dependent lifetime. (a) SPCM count rates since the beginning of the probe $D1$ transmitted detection pulse for several probe intensities, after a π pulse preparing the $|R\rangle$ superatom state. The dashed lines are the best-fit exponential decay with a lifetime τ_R . (b) $|R\rangle$ decay rate $1/\tau_R$ as a function of the transmitted probe SPCM rate ϕ_G with the $|G\rangle$ state. Colored data points correspond to the curves of panel (a) with identical colors and markers. The dashed line shows the best linear fit to the data. Error bars represent the standard error.

varied here while the EIT control Rabi frequency is constant at a value of $\Omega_c/(2\pi) = 14$ MHz. Data are fitted by an exponential decay function $\phi_G(1 - b \exp(-t/\tau_R))$, where the steady-state value ϕ_G is the transmitted probe SPCM rate with the $|G\rangle$ state, measured without applying a π pulse on the superatom. The fitted parameters b, τ_R account, respectively, for the initial transmission level $1 - b \sim 10\%$, due to residual transmission flux and residual preparation error of the $|R\rangle$ state, and for the lifetime τ_R of the Rydberg excitation of state $|R\rangle$.

The evolution of the decay rate $1/\tau_R$ with the transmission probe $D1$ intensity, quantified by the SPCM rate ϕ_G , is well fitted by a linear function $\phi_G/a + 1/\tau_{R,0}$ as shown in Fig. 4(b). The residual lifetime at zero probe $\tau_{R,0} = 0.31 \pm 0.06$ ms is close to the 0.426-ms calculated [30] lifetime of the 109S state in our 300-K environment. This fact indicates that the strong EIT control field, coupled to the 78S state, weakly influences the 109S lifetime. This contrasts with detection schemes using interactions between neighboring Rydberg levels [26], which can be mixed by residuals dc electric fields. However, in the presence of probe light, we observe an increase of the decay

rate. At probe intensity levels of $\phi_G \sim 1$ MHz—which are necessary to obtain a low probability to detect zero photons for the $|G\rangle$ state in a window of about $10 \mu\text{s}$, much shorter than the residual lifetime $\tau_{R,0}$ —the lifetime is approximately inversely linear to ϕ_G with $\tau_R \simeq a/\phi_G$, where $a = 29 \pm 1 \mu\text{s MHz}$.

APPENDIX C: MODELS FOR THE DETECTIONS

Here, we present expressions of the fitting functions of the detection histograms.

We start with the model used to fit the data in Fig. 2(e) of the detection in transmission measured by the SPCM. When the superatom is in the ground state $|G\rangle$, the distribution of photon number n is a Poisson law, $\mathcal{P}_G(n) = \mathcal{P}(n, t_i\phi_G) = e^{-t_i\phi_G} (t_i\phi_G)^n / n!$, parametrized by the mean detected photon number $t_i\phi_G$, with ϕ_G the photon rate and t_i the integration time. For the superatom in the Rydberg state $|R\rangle$, the distribution can be split into two parts to take into account quantum jumps. First, the probability distribution without a jump is also a Poisson law $\mathcal{P}(n, t_i\phi_R)$ with a residual photon number $t_i\phi_R$, where ϕ_R is the photon flux with a blockade. The probability of this event is e^{-t_i/τ_R} , where τ_R is the Rydberg lifetime. For a quantum jump at $t < t_i$, the distribution is the sum of two Poisson laws—the first with a mean photon number $t\phi_R$ and the second after the jump with a mean value $(t_i - t)\phi_G$. By the stability of the Poisson law under addition, this probability distribution is also a Poisson law with a mean photon number $n_J(t) = t\phi_R + (t_i - t)\phi_G$. As a result, the full distribution is

$$\mathcal{P}_R(n) = \mathcal{P}(n, t_i\phi_R)e^{-t_i/\tau_R} + \int_0^{t_i} \mathcal{P}(n, n_J(t)) \frac{e^{-t/\tau_R}}{\tau_R} dt. \quad (\text{C1})$$

Finally, the probability distribution with a preparation efficiency η_R is given by $\eta_R \mathcal{P}_R(n) + (1 - \eta_R) \mathcal{P}_G(n)$.

We now move to the fitting functions for the data in Fig. 3(d), where the superatom's state is measured by monitoring the field reflected off of the cavity using a homodyne detector. When the superatom lies in the ground state $|G\rangle$, the X quadrature is a Gaussian, $\mathcal{G}_G(X) = \mathcal{G}(X, \bar{X}_G)$, with a rms width $\sigma = 1/\sqrt{2}$, centered on $\bar{X}_G = -\sqrt{2t_i\phi\mathcal{R}_G}$, where ϕ is the photon flux at cavity input and \mathcal{R}_G is the reflectivity when the superatom is in $|G\rangle$. In the absence of a quantum jump, the distribution associated with the superatom prepared in the Rydberg state is also a Gaussian centered on $\bar{X}_R = \sqrt{2t_i\phi\mathcal{R}_R}$, where \mathcal{R}_R is the associated reflectivity. For a quantum jump at $t < t_i$, the mean value of the quadrature is then $\bar{X}_J(t) = -(t_i - t)\sqrt{2\phi\mathcal{R}_G/t_i} + t\sqrt{2\phi\mathcal{R}_R/t_i}$. Because it is the sum of two Gaussian random variables, the distribution remains Gaussian, with a mean $\bar{X}_J(t)$ and a width of

$1/\sqrt{2}$. The complete distribution for the superatom in $|R\rangle$ is then

$$\mathcal{G}_R(X) = \mathcal{G}(X, \bar{X}_R)e^{-t_i/\tau_R} + \int_0^{t_i} \mathcal{G}(X, \bar{X}_J(t)) \frac{e^{-t/\tau_R}}{\tau_R} dt. \quad (\text{C2})$$

Finally, the probability distribution with a preparation efficiency η_R is given by $\eta_R \mathcal{G}_R(n) + (1 - \eta_R) \mathcal{G}_G(n)$.

APPENDIX D: EIT TRANSMISSION AND REFLECTION SPECTRA

Many of the physical parameters of our system are estimated from the EIT transmission and reflection spectra in the weak-excitation regime, where interactions can be neglected. The system can then be modeled by N atoms with a ground state $|g = 5S_{1/2}, F = 1, m_F = 1\rangle$, an intermediate state $|e = 5P_{1/2}, F = 2, m_F = 2\rangle$, and a Rydberg state $|r = 78S_{1/2}, J = 1/2, m_J = 1/2, I = 3/2, m_I = 3/2\rangle$, with respective angular transition frequencies ω_{ge} and ω_{er} . The n th atom, described by operators $\hat{\sigma}_{ij}^{(n)} = |i\rangle_n \langle j|_n$ in this basis, is coupled with a constant g_n to the cavity mode. This mode, described by the photon annihilation operator \hat{a} , has an angular frequency ω_a near resonant with ω_{ge} and is driven by a weak coherent probe with an amplitude α and an angular frequency ω . A laser beam with an angular frequency ω' close to ω_{er} and a Rabi frequency $\Omega_c/(2\pi)$, assumed to be the same for all atoms, couples $|e\rangle$ and $|r\rangle$.

In the rotating frame, the Hamiltonian of the system is

$$\begin{aligned} \frac{\hat{H}}{\hbar} = & -\delta_a \hat{a}^\dagger \hat{a} - \delta_e \sum_{n=1}^N \hat{\sigma}_{ee}^{(n)} - \delta_r \sum_{n=1}^N \hat{\sigma}_{rr}^{(n)} \\ & + \sum_{n=1}^N g_n \left(\hat{a} \hat{\sigma}_{eg}^{(n)} + \hat{a}^\dagger \hat{\sigma}_{ge}^{(n)} \right) + \frac{\Omega_c}{2} \sum_{n=1}^N \left(\hat{\sigma}_{er}^{(n)} + \hat{\sigma}_{re}^{(n)} \right) \\ & + i\alpha \sqrt{2\kappa_0} (\hat{a}^\dagger - \hat{a}), \end{aligned} \quad (\text{D1})$$

where $\delta_a = \omega - \omega_a$, $\delta_e = \omega - \omega_{ge}$, $\delta_r = \omega + \omega' - \omega_{ge} - \omega_{er}$, and κ_0 is the field decay rate through the output coupler. Decay terms lead to the master equation

$$\begin{aligned} \frac{d\hat{\rho}}{dt} = & -\frac{i}{\hbar} [\hat{H}, \hat{\rho}] + \mathcal{D}[\sqrt{2\kappa}\hat{a}]\hat{\rho} + \sum_{n=1}^N \mathcal{D}[\sqrt{2\gamma}\hat{\sigma}_{ge}^{(n)}]\hat{\rho} \\ & + \sum_{n=1}^N \mathcal{D}[\sqrt{2\gamma_r}\hat{\sigma}_{GR}^{(n)}]\hat{\rho}, \end{aligned} \quad (\text{D2})$$

$$\mathcal{D}[\hat{A}]\hat{\rho} = \hat{A}\hat{\rho}\hat{A}^\dagger - \frac{1}{2}\hat{A}^\dagger\hat{A}\hat{\rho} - \frac{1}{2}\hat{\rho}\hat{A}^\dagger\hat{A}, \quad (\text{D3})$$

where κ is the total cavity field decay rate while γ and γ_r are the respective decay rates of the coherences $\hat{\sigma}_{ge}$ and $\hat{\sigma}_{gr}$.

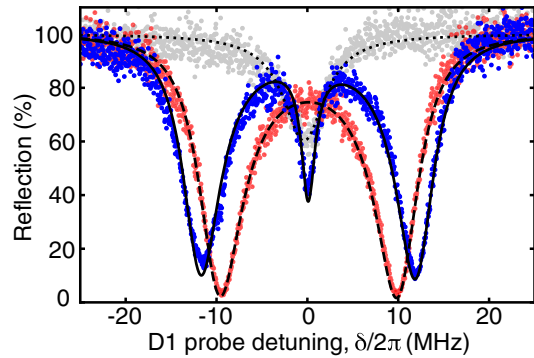


FIG. 5. Reflection spectra. The reflection of the $D1$ probe, as a function of the probe detuning, is measured with a SPCM and normalized to the impinging power (light gray). With the strongly coupled atomic ensemble, we observe the vacuum Rabi splitting of the two reflection dips (red). Adding the EIT control beam, with Rabi frequency $\Omega_c/(2\pi) = 13$ MHz, creates a reflection dip at resonance (blue).

In the linear response limit $\alpha \rightarrow 0$, we can neglect the populations of the cavity mode and of the excited states. By deriving and solving the steady-state Bloch equations, we obtain the transmission \mathcal{T} (normalized to the bare cavity maximum) and the reflectivity \mathcal{R} , involving the complex detunings $\Delta_a = \delta_a + i\kappa$, $\Delta_e = \delta_e + i\gamma$, $\Delta_r = \delta_r + i\gamma_r$ and the collective coupling $g = \sqrt{\sum_n g_n^2}$:

$$\mathcal{T} = \left| \frac{\kappa}{\Delta_a - g^2/[\Delta_e - \Omega_c^2/(4\Delta_r)]} \right|^2, \quad (\text{D4})$$

$$\mathcal{R} = \left| 1 - \frac{i2\kappa_0}{\Delta_a - g^2/[\Delta_e - \Omega_c^2/(4\Delta_r)]} \right|^2. \quad (\text{D5})$$

Setting $\Omega_c = 0$ or $g = 0$ yields the vacuum Rabi splitted spectrum or the Lorentzian bare cavity spectrum, respectively.

These expressions are fitted to the spectra observed with weak probes and presented in Fig. 1(c) for the transmission and in Fig. 5 for the reflection. They provide the values of cavity decay, coupling strength, Rabi frequencies, photon extraction efficiency, transmission, and reflectivity given in the main text. Additionally, they provide the intrinsic linewidth of the Rydberg state $\gamma_r/(2\pi) = 0.12$ MHz. Keeping this linewidth to a minimum by cooling the atomic motion and compensating stray electric fields with a set of electrodes is essential for achieving high transparency, which is critical for our applications.

[1] S. Haroche and J.-M. Raimond, *Exploring the Quantum: Atoms, Cavities, and Photons* (Oxford University Press, Oxford, 2006), 10.1093/acprof:oso/9780198509141.001.0001.

- [2] M. Devoret and R. Schoelkopf, *Superconducting Circuits for Quantum Information: An Outlook*, *Science* **339**, 1169 (2013).
- [3] R. J. Thompson, G. Rempe, and H. J. Kimble, *Observation of Normal-Mode Splitting for an Atom in an Optical Cavity*, *Phys. Rev. Lett.* **68**, 1132 (1992).
- [4] J. P. Reithmaier, G. Sęk, A. Löffler, C. Hofmann, S. Kuhn, S. Reitzenstein, L. V. Keldysh, V. D. Kulakovskii, T. L. Reinecke, and A. Forchel, *Strong Coupling in a Single Quantum Dot-Semiconductor Microcavity System*, *Nature (London)* **432**, 197 (2004).
- [5] T. Yoshie, A. Scherer, J. Hendrickson, G. Khitrova, H. M. Gibbs, G. Rupper, C. Ell, O. B. Shchekin, and D. G. Deppe, *Vacuum Rabi Splitting with a Single Quantum Dot in a Photonic Crystal Nanocavity*, *Nature (London)* **432**, 200 (2004).
- [6] A. Reiserer and G. Rempe, *Cavity-Based Quantum Networks with Single Atoms and Optical Photons*, *Rev. Mod. Phys.* **87**, 1379 (2015).
- [7] P. Lodahl, S. Mahmoodian, and S. Stobbe, *Interfacing Single Photons and Single Quantum Dots with Photonic Nanostructures*, *Rev. Mod. Phys.* **87**, 347 (2015).
- [8] B. Hacker, S. Welte, G. Rempe, and S. Ritter, *A Photon-Photon Quantum Gate Based on a Single Atom in an Optical Resonator*, *Nature (London)* **536**, 193 (2016).
- [9] B. Hacker, S. Welte, S. Daiss, A. Shaukat, S. Ritter, L. Li, and G. Rempe, *Deterministic Creation of Entangled Atom-Light Schrödinger-Cat States*, *Nat. Photonics* **13**, 110 (2019).
- [10] O. Firstenberg, C. S. Adams, and S. Hofferberth, *Nonlinear Quantum Optics Mediated by Rydberg Interactions*, *J. Phys. B* **49**, 152003 (2016).
- [11] C. Murray and T. Pohl, *Quantum and Nonlinear Optics in Strongly Interacting Atomic Ensembles*, *Adv. At. Mol. Opt. Phys.* **65**, 321 (2016).
- [12] J. D. Pritchard, D. Maxwell, A. Gauguet, K. J. Weatherill, M. P. A. Jones, and C. S. Adams, *Cooperative Atom-Light Interaction in a Blocked Rydberg Ensemble*, *Phys. Rev. Lett.* **105**, 193603 (2010).
- [13] Y. O. Dudin and A. Kuzmich, *Strongly Interacting Rydberg Excitations of a Cold Atomic Gas*, *Science* **336**, 887 (2012).
- [14] T. Peyronel, O. Firstenberg, Q.-Y. Liang, S. Hofferberth, A. V. Gorshkov, T. Pohl, M. D. Lukin, and V. Vuletić, *Quantum Nonlinear Optics with Single Photons Enabled by Strongly Interacting Atoms*, *Nature (London)* **488**, 57 (2012).
- [15] D. Maxwell, D. J. Szwer, D. Paredes-Barato, H. Busche, J. D. Pritchard, A. Gauguet, K. J. Weatherill, M. P. A. Jones, and C. S. Adams, *Storage and Control of Optical Photons Using Rydberg Polaritons*, *Phys. Rev. Lett.* **110**, 103001 (2013).
- [16] H. Gorniaczyk, C. Tresp, J. Schmidt, H. Fedder, and S. Hofferberth, *Single-Photon Transistor Mediated by Inter-state Rydberg Interactions*, *Phys. Rev. Lett.* **113**, 053601 (2014).
- [17] D. Tiarks, S. Baur, K. Schneider, S. Dürr, and G. Rempe, *Single-Photon Transistor Using a Förster Resonance*, *Phys. Rev. Lett.* **113**, 053602 (2014).
- [18] V. Parigi, E. Bimbard, J. Stanojevic, A. J. Hilliard, F. Nogrette, R. Tualle-Brouri, A. Ourjoumstev, and P. Grangier,

- Observation and Measurement of Interaction-Induced Dispersive Optical Nonlinearities in an Ensemble of Cold Rydberg Atoms*, *Phys. Rev. Lett.* **109**, 233602 (2012).
- [19] O. Firstenberg, T. Peyronel, Q.-Y. Liang, A. V. Gorshkov, M. D. Lukin, and V. Vuletić, *Attractive Photons in a Quantum Nonlinear Medium*, *Nature (London)* **502**, 71 (2013).
- [20] Q.-Y. Liang, A. V. Venkatramani, S. H. Cantu, T. L. Nicholson, M. J. Gullans, A. V. Gorshkov, J. D. Thompson, C. Chin, M. D. Lukin, and V. Vuletić, *Observation of Three-Photon Bound States in a Quantum Nonlinear Medium*, *Science* **359**, 783 (2018).
- [21] N. Stiesdal, J. Kumlin, K. Kleinbeck, P. Lunt, C. Braun, A. Paris-Mandoki, C. Tresp, H. P. Büchler, and S. Hofferberth, *Observation of Three-Body Correlations for Photons Coupled to a Rydberg Superatom*, *Phys. Rev. Lett.* **121**, 103601 (2018).
- [22] D. Tiarks, S. Schmidt-Eberle, T. Stolz, G. Rempe, and S. Dürr, *A Photon-Photon Quantum Gate Based on Rydberg Interactions*, *Nat. Phys.* **15**, 124 (2019).
- [23] M. Schlagmüller, T. C. Liebisch, F. Engel, K. S. Kleinbach, F. Böttcher, U. Hermann, K. M. Westphal, A. Gaj, R. Löw, S. Hofferberth, T. Pfau, J. Pérez-Ríos, and C. H. Greene, *Ultracold Chemical Reactions of a Single Rydberg Atom in a Dense Gas*, *Phys. Rev. X* **6**, 031020 (2016).
- [24] D. Tiarks, S. Schmidt, G. Rempe, and S. Dürr, *Optical π Phase Shift Created with a Single-Photon Pulse*, *Sci. Adv.* **2**, e1600036 (2016).
- [25] N. Jia, N. Schine, A. Georgakopoulos, A. Ryou, L. W. Clark, A. Sommer, and J. Simon, *A Strongly Interacting Polaritonic Quantum Dot*, *Nat. Phys.* **14**, 550 (2018).
- [26] W. Xu, A. V. Venkatramani, S. H. Cantú, T. Šumarac, V. Klüsener, M. D. Lukin, and V. Vuletić, *Fast Preparation and Detection of a Rydberg Qubit Using Atomic Ensembles*, *Phys. Rev. Lett.* **127**, 050501 (2021).
- [27] C.-W. Yang, J. Li, M.-T. Zhou, X. Jiang, X.-H. Bao, and J.-W. Pan, *Single-Shot Measurement of a Rydberg Superatom via Collective Photon Burst*, [arXiv:2106.10858](https://arxiv.org/abs/2106.10858).
- [28] N. L. R. Spong, Y. Jiao, O. D. W. Hughes, K. J. Weatherill, I. Lesanovsky, and C. S. Adams, *Collectively Encoded Rydberg Qubit*, *Phys. Rev. Lett.* **127**, 063604 (2021).
- [29] S. Das, A. Grankin, I. Iakoupov, E. Brion, J. Borregaard, R. Boddeda, I. Usmani, A. Ourjoumtsev, P. Grangier, and A. S. Sørensen, *Photonic Controlled-Phase Gates through Rydberg Blockade in Optical Cavities*, *Phys. Rev. A* **93**, 040303(R) (2016).
- [30] N. Šibalić, J. Pritchard, C. Adams, and K. Weatherill, *ARC: An Open-Source Library for Calculating Properties of Alkali Rydberg Atoms*, *Comput. Phys. Commun.* **220**, 319 (2017).
- [31] Y. O. Dudin, L. Li, F. Bariani, and A. Kuzmich, *Observation of Coherent Many-Body Rabi Oscillations*, *Nat. Phys.* **8**, 790 (2012).
- [32] K. M. Beck, M. Hosseini, Y. Duan, and V. Vuletić, *Large Conditional Single-Photon Cross-Phase Modulation*, *Proc. Natl. Acad. Sci. U.S.A.* **113**, 9740 (2016).
- [33] L. W. Clark, N. Schine, C. Baum, N. Jia, and J. Simon, *Observation of Laughlin States Made of Light*, *Nature (London)* **582**, 41 (2020).
- [34] D. Paredes-Barato and C. S. Adams, *All-Optical Quantum Information Processing Using Rydberg Gates*, *Phys. Rev. Lett.* **112**, 040501 (2014).
- [35] M. Khazali, C. R. Murray, and T. Pohl, *Polariton Exchange Interactions in Multichannel Optical Networks*, *Phys. Rev. Lett.* **123**, 113605 (2019).
- [36] T. Stolz, H. Hegels, M. Winter, B. Röhr, Y.-F. Hsiao, L. Husel, G. Rempe, and S. Dürr, following paper, *Quantum-Logic Gate between Two Optical Photons with an Average Efficiency above 40%*, *Phys. Rev. X* **12**, 021035 (2022).
- [37] D. Schrader, S. Kuhr, W. Alt, M. Müller, V. Gomer, and D. Meschede, *An Optical Conveyor Belt for Single Neutral Atoms*, *Appl. Phys. B* **73**, 819 (2001).
- [38] S. E. Hamann, D. L. Haycock, G. Klose, P. H. Pax, I. H. Deutsch, and P. S. Jessen, *Resolved-Sideband Raman Cooling to the Ground State of an Optical Lattice*, *Phys. Rev. Lett.* **80**, 4149 (1998).
- [39] A. J. Kerman, V. Vuletić, C. Chin, and S. Chu, *Beyond Optical Molasses: 3D Raman Sideband Cooling of Atomic Cesium to High Phase-Space Density*, *Phys. Rev. Lett.* **84**, 439 (2000).